arXiv:2210.01874v1 [physics.atom-ph] 4 Oct 2022

Driving alkali Rydberg transitions with a phase-modulated optical lattice

R. Cardman* and G. Raithel
Department of Physics, University of Michigan, Ann Arbor, MI 48109, USA

(Dated: October 6, 2022)

We develop and demonstrate a spectroscopic method for Rydberg-Rydberg transitions using a phase-controlled and -modulated, standing-wave laser field focused on a cloud of cold ^{85}Rb Rydberg atoms. The method is based on the ponderomotive ($\mathbf{A}^2$) interaction of the Rydberg electron, which has less-restrictive selection rules than electric-dipole couplings, allowing us to probe both $nS_{1/2} \rightarrow nP_{1/2}$ and $nS_{1/2} \rightarrow (n+1)S_{1/2}$ transitions in first-order. Without any need to increase laser power, third and fourth-order sub-harmonic drives are employed to access Rydberg transitions in the 40 to 70 GHz frequency range using widely-available optical phase modulators in the Ku-band (12 to 18 GHz). Measurements agree well with simulations based on the model we develop. The spectra have prominent Doppler-free, Fourier-limited components. The method paves the way for optical Doppler-free high-precision spectroscopy of Rydberg-Rydberg transitions and for spatially-selective qubit manipulation with μm-scale resolution in Rydberg-based simulators and quantum computers.

Innovations in quantum technologies based on Rydberg atoms rely on manipulation of their internal states. Technologies include simulators exploring quantum phase transitions and walks [1–5], quantum processors [6, 7], and Rydberg-atom-based sensors [8, 9]. It is often beneficial to trap and arrange the Rydberg atoms using tightly focused laser beams, optical-tweezer arrays, or optical lattices to configure such systems. Coherent interactions on Rydberg qubits can be performed with rf to sub-THz radiation. The diffraction limit of $\gtrsim 1$ mm then potentially disallows single-qubit operations or short-distance gates. One method to achieve spatial selectivity of Rydberg transitions on a μm-scale, required in many of these applications, is through optical addressing of isolated-core excitations (ICE) in alkaline-earth atoms [10–16], but limitations of the ICE method include autoionization of low-l Rydberg states due to Rydberg-ICE interaction. Also, ICE addressing is not practical in commonly-used alkali atomic species. Here we explore direct optical drives of Rydberg transitions as a more widely-applicable method with μm-scale spatial selectivity.

Rydberg transitions can be directly optically driven through ponderomotive interactions, $e^2A^2/2m_e$, where $\mathbf{A}$ is the vector potential of the driving laser [17]. Driving ponderomotive transitions entails generating an optical intensity gradient that is spatially varying within the Rydberg-electron's wavefunction, and modulating the intensity distribution at (a sub-harmonic of) the atomic transition frequency. Suitable control of the modulation frequency leads to transitions between Rydberg states. Ponderomotive transitions in modulated optical lattices typically have a Doppler-free component with an interaction-time-limited linewidth [18]. Ponderomotive Rydberg atom spectroscopy has been previously performed by amplitude-modulating an optical lattice, allowing transitions between states $\{|0\rangle, |1\rangle\}$ of equal parity, *i. e.* $\langle 0|\hat{\Pi}|0\rangle = \langle 1|\hat{\Pi}|1\rangle$ [17]. Odd-parity ($\langle 0|\hat{\Pi}|0\rangle = -\langle 1|\hat{\Pi}|1\rangle$) transitions are forbidden for this drive method, unless the modulation is detuned from resonance by the lattice trap-oscillation frequency [18, 19] and the atom's motional quantum state ν is changed, which is generally undesirable. On the other hand, Rydberg quantum simulators operating on electric-dipole interactions between atoms sometimes require the preparation of a mixed-parity system (*e. g.*, nS and $n'P$ atoms [3, 5, 20]). Harnessing optically-driven ponderomotive transitions for Rydberg quantum simulators therefore requires a generalization that will allow local odd-parity transitions without motional excitation of the atoms.

In this work, we demonstrate optically-driven alkali Rydberg transitions using an optical lattice that is phased-modulated at a sub-harmonic $\omega_m = \omega_0/q$ of the atomic transition frequency ω_0, with an integer sub-harmonic order q. The transitions occur in first-order perturbation theory even at large q, no intermediate atomic states are involved, and the required optical-field strengths do not increase with q. Optical setup, selection rules, and transition Rabi frequencies in phase-modulated lattices fundamentally differ from the case of amplitude modulation. Phase modulation of the laser allows both odd- and even-parity transitions without change of the motional number ν. Here we perform ponderomotive optical spectroscopy of ^{85}Rb transitions by scanning the lattice phase-modulation frequency ω_m over a sub-harmonic of the atomic resonance, $\omega_m \approx \omega_0/q$. A one-dimensional lattice with counter-propagating laser beams is used (wavelength $\lambda = 2\pi c/\omega_L = 2\pi/k_L = 1064$ nm), and, in a single setup, both odd- $nS_{1/2} \rightarrow nP_{1/2}$ ($\langle 0|\hat{\Pi}|0\rangle = -\langle 1|\hat{\Pi}|1\rangle$) and even-parity $nS_{1/2} \rightarrow (n+1)S_{1/2}$ ($\langle 0|\hat{\Pi}|0\rangle = \langle 1|\hat{\Pi}|1\rangle$) spectra are studied.

The lattice is constituted of three co-linear beams, a pair of left- and right-propagating unmodulated beams with optical fields $\mathbf{E}_u^{(i)}$ and $\mathbf{E}_u^{(r)}$, plus a beam with field $\mathbf{E}_m^{(i)}$ that is phase-modulated at ω_m and co-aligned with $\mathbf{E}_u^{(i)}$. These fields are, in that order,

$$\mathbf{E}_u^{(i)}(\mathbf{R}_0+\mathbf{r}_e,t)=\hat{\epsilon}^{(i)}\mathcal{E}_u^{(i)}(\mathbf{R}_0)\cos\left[k_L(Z_0+z_e)-\omega_L t+\eta_2(t)\right],$$
$$\mathbf{E}_u^{(r)}(\mathbf{R}_0+\mathbf{r}_e,t)=\hat{\epsilon}^{(r)}\mathcal{E}_u^{(r)}(\mathbf{R}_0)\cos\left[k_L(Z_0+z_e)+\omega_L t\right],$$
$$\mathbf{E}_m^{(i)}(\mathbf{R}_0+\mathbf{r}_e,t)=\hat{\epsilon}^{(i)}\mathcal{E}_m^{(i)}(\mathbf{R}_0)\cos\left[k_L(Z_0+z_e)-\omega_L t+\eta_0+\eta_1\cos\left(\omega_m\Delta s/c-\omega_m t\right)+\eta_2(t)\right], \quad (1)$$

where $\mathbf{R}_0$ is the atom's center-of-mass (CM) vector, $\mathbf{r}_e$ is the Rydberg-electron vector operator, $\hat{\epsilon}^{(i)},\hat{\epsilon}^{(r)}$ are polarization vectors of the right- (i) and left-propagating (r) beams, η_0 accounts for spurious phase offsets between modulated and unmodulated beams, η_1 is the modulation amplitude, and Δs is the path length of the modulated beam from the phase modulator to the atoms. The step-function phase jump $\eta_2(t)$ is optionally applied to both i-beams immediately after laser-excitation of the Rydberg atoms in the lattice. The phase jump, if applied, effects a sudden translation of the lattice relative to the atoms before the spectroscopic sequence. In our experiments, $\mathcal{E}_m^{(i)}$ is about one-tenth the magnitudes of $\mathcal{E}_u^{(i)}$ and $\mathcal{E}_u^{(r)}$. The three beams are overlapped and focused down to a waist of ~ 15 μm in the center of a ^{85}Rb optical molasses (see Supplement for a detailed schematic of the optics).

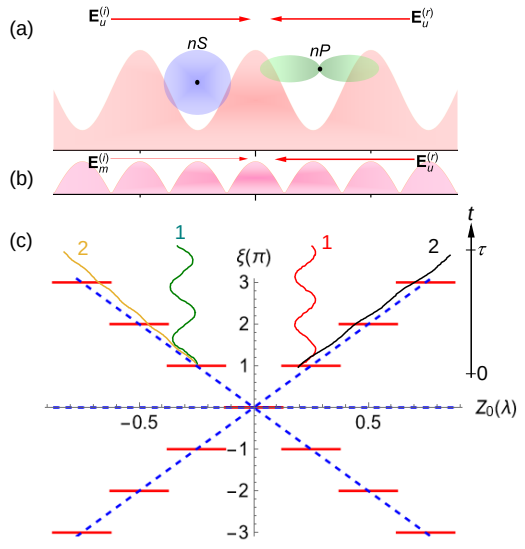


FIG. 1. (a) Qualitative sketch of the trapping potential, $U_0\cos(2k_LZ_0)+U_{ofs}$, created by $\mathbf{E}_u^{(i)}$ and $\mathbf{E}_u^{(r)}$, vs. CM position Z_0, with two Rydberg atoms roughly to scale. (b) Qualitative magnitude of the atom-field drive, $|U_{AF}|(Z_0)$, formed by $\mathbf{E}_m^{(i)}$ and $\mathbf{E}_u^{(r)}$. (c) Phase of the atom-field drive, $\xi(Z_0)$ (red solid), in comparison with phase functions that would apply to Raman transitions (blue dashed). Several trapped (1) and un-trapped (2) atom trajectories vs. time, $Z_0(t)$, are plotted on top (details, see text).

The ponderomotive interaction is given by the mean-square of the field in Eq. 1, averaged in time over many optical cycles and a small fraction of $2\pi/\omega_m$. One finds a time-independent component that constitutes a positive optical-lattice atom-trapping potential with an offset, $U_0\cos(2k_LZ_0)+U_{ofs}$, and a time-dependent atom-field interaction potential, $U_{AF}(Z_0,t)$, that couples states $|0\rangle$ and $|1\rangle$. For the latter we find

$$U_{AF}(Z_0,t)=\frac{\hbar}{2}\Omega_{q,0}|\cos(2k_LZ_0)|e^{i(\xi-q\omega_m t)}|1\rangle\langle 0|+\text{h.c.}, \quad (2)$$

where $\Omega_{q,0}|\cos(2k_LZ_0)|$ is the Z_0-dependent Rabi-frequency magnitude for the q-th sub-harmonic drive, and ξ is the Z_0-dependent phase of the atom-field coupling. The trapping function, $|U_{AF}|$, and the phase function $\xi(Z_0)$ are plotted in Fig. 1. The staircase shape of $\xi(Z_0)$ is unique to ponderomotive lattice-modulation drives and gives rise to a novel paradigm of Doppler-free spectroscopy. We will develop this insight after presentation of the experimental data.

In our first demonstration of lattice phase-modulation drive, we prepare ^{85}Rb atoms in $|0\rangle=|46S_{1/2}\rangle$ from a sample of ground-state atoms laser-cooled and localized near local maxima of the 1064-nm lattice intensity using off-resonant ($\Delta=+140$ MHz), two-photon laser excitation with 780- and 480-nm light. It is $\eta_0=\eta_2=0$, while η_1 is pulsed on from zero to $1.3(3)\pi$ for the duration of the drive, $\tau=6$ μs. We measure the $|0\rangle\rightarrow|1\rangle=|46P_{1/2}\rangle$ transition, which has a lattice-free transition frequency $\omega_0/2\pi=39.121294$ GHz. We use a sub-harmonic order $q=3$, and the modulation frequency $\omega_m/2\pi$ is scanned from 13.040211 GHz to 13.040633 GHz in steps of 3 kHz. Notably, the $q=3$ sub-harmonic drive allows us to project the Rydberg transition (frequency $\sim$39 GHz) into the Ku-band (12-18 GHz), for which efficient optical fiber modulators exist. Internal-state populations of $|0\rangle$ and $|1\rangle$ are counted with state-selective field ionization (SSFI) [21]. Fig. 2 shows the spectrum with an overlapped numerical simulation (for details of the simulation, see Supplement).

The peak Rabi frequency $\Omega_{q=3,0}$ in Eq. 2 for the case of Fig. 2 has the following dependence on experimental parameters,

$$\Omega_{q=3,0}=-\frac{\alpha_e(\omega_L)}{\hbar}\mathcal{E}_m^{(i)}\mathcal{E}_u^{(r)}(\hat{\epsilon}^{(i)}\cdot\hat{\epsilon}^{(r)})\times\langle 1|\sin(2k_Lz_e)|0\rangle J_3(\eta_1), \quad (3)$$

where $\alpha_e(\omega_L)$ is the free-electron polarizability for light at angular frequency ω_L. This quantity is -545 atomic units for 1064 nm. For the spectrum in Fig. 2, we estimate $\Omega_{3,0}\sim 2\pi\times 70$ kHz and $U_0\sim h\times 2.5$ MHz by

comparing simulated and experimental signals. When $\mathbf{E}_u^{(r)}$ is extinguished, the Rabi frequency vanishes, as the intensity gradient in the laser field no longer varies within the Rydberg-electron wavefunction. This test proves that there is no population transfer into $|1\rangle$ by means of higher-order $\mathbf{A}\cdot\mathbf{p}$ interactions originating from microwave leakage, and that the observed transfer into $|1\rangle$ is entirely due to the $\mathbf{A}^2$ interaction in the modulated optical lattice.

The sub-harmonic order q does not appear in the atomic matrix element $\langle 1|\sin(2k_L z_e)|0\rangle$ in Eq. 3. For this reason, sub-harmonic ponderomotive lattice phase-modulation spectroscopy does not require higher intensity laser beams with increasing order q. Hence, the frequency reduction afforded by the sub-harmonic drive does not come at the expense of larger ac shifts and lattice-induced photo-ionization rates. This benefit stands in contrast with multi-photon microwave spectroscopy, where both field intensity required and ac shifts increase drastically with q. From the Bessel function $J_q(\eta_1)$ in Eq. 3, it is apparent that sub-harmonic ponderomotive lattice phase-modulation spectroscopy comes with two minor penalties: (1) while no increase in optical power is required, a moderately higher microwave power is needed to drive the phase modulator, and (2) the maximum achievable atom-field coupling exhibits a *mild* drop-off as a function of sub-harmonic order q. These small penalties are heavily outweighed by the massive expansion of accessible Rydberg-transition frequency ranges afforded by high-order sub-harmonic drives.

Three peaks appear in the spectrum in Fig. 2. The central peak is free of Doppler shifts, conserves the motional state ν, and has a linewidth of $\sim$ 200 kHz, near the Fourier limit. This peak corresponds with atoms experiencing a constant phase ξ throughout the interaction time; *i.e.*, the atoms remain within a distance of $\lesssim 0.125\lambda$ from a given lattice-intensity minimum (Trajectories 1 in Fig. 1). The broad sidebands at about $\pm$300 kHz correspond to Doppler shifts of atoms traveling over many lattice wells (trajectories 2 in Fig. 1). Those atoms move across multiple steps of $\xi(Z_0)$ at a roughly constant velocity v along z, and exhibit a Doppler shift according to the time average

$$\langle\dot{\xi}\rangle \simeq \frac{d\xi}{dZ_0}\langle v\rangle \simeq \frac{4\pi}{\lambda}\langle v\rangle \quad = 2k_L\langle v\rangle. \tag{4}$$

There, we use the fact that the average slope of the step functions in Fig. 1 is $d\xi/dZ_0 \simeq 4\pi/\lambda$.

The strength of the Doppler-shifted features in Fig. 2 relative to the Doppler-free line follows from the Rydberg excitation scheme. Rb $|5S_{1/2}\rangle$ atoms, which have a positive ac polarizability, are laser-cooled and trapped at the lattice intensity maxima. Rydberg excitation lasers are tuned to the ground-Rydberg resonance at the lattice intensity maxima. Because the ponderomotive force generally repels Rydberg atoms from regions of high laser

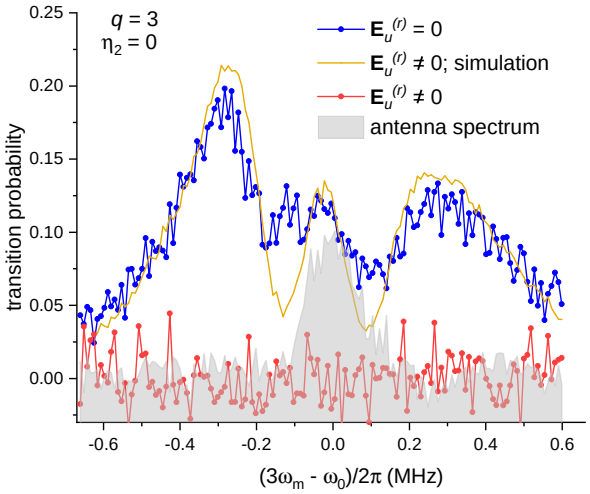


FIG. 2. Population in $|1\rangle$ as ω_m is scanned over $\omega_0/3$ in 3 kHz steps. Here $|0\rangle = |46S_{1/2}\rangle$ and $|1\rangle = |46P_{1/2}\rangle$. The blue signal is an average of 10 individual ω_m-scans with 400 measurements each and $\mathbf{E}_u^{(r)}$ unblocked. The gold line is a corresponding numerical simulation. The pink signal shows the population in $|1\rangle$ when $\mathbf{E}_u^{(r)}$ is blocked for an average of 4 individual scans with 400 measurements each. The shaded spectrum shows a single-photon microwave drive using a horn antenna without any 1064-nm light. In all spectra, $\tau = 6$ μs.

intensity, most Rydberg atoms prepared in this way are not trapped along z and traverse over multiple lattice periods during the atom-field interaction, giving rise to the strong Doppler-shifted sidebands in Fig. 2. A minority of the prepared Rydberg atoms is barely trapped in the Rydberg-atom lattice, which suffices to produce the observed Doppler-free peak. The red-shift of this peak relative to the field-free atomic resonance reflects a small Rydberg-state-dependent differential light shift.

To enhance the visibility of the Doppler-free peak relative to the Doppler-shifted side peaks, we suddenly shift the optical lattice in z by $\lambda/4$ immediately after Rydberg-atom preparation. The shift, implemented by a phase step function $\eta_2(t)$ with step size π in Eq. 1, places the atoms near a lattice intensity minimum during atom-field interaction [22]. Most atoms are then trapped while being probed, and the Doppler-free peak becomes larger than the side peaks. In Fig. 3 we show a spectrum for the same transition as in Fig. 2, with the sudden $\lambda/4$ lattice translation applied.

While the Doppler-shifted sidebands in Fig. 2 are suppressed, as expected, they are stronger in the measurement than in the simulation result. We attribute this disagreement to the fact that the lattice translation is not perfectly instantaneous. Classically, the Rydberg atoms, which are initially excited near a maximum of the Rydberg-atom trapping potential, begin rolling down the

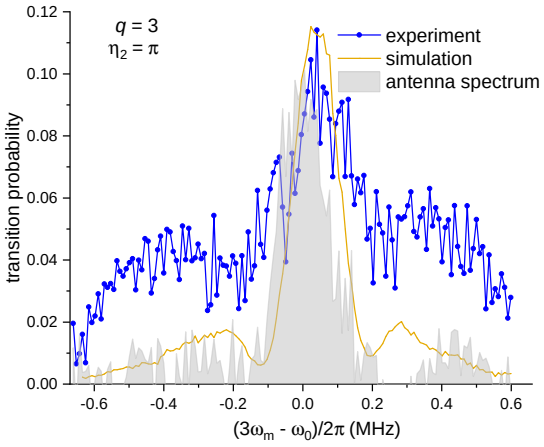


FIG. 3. Spectrum measured for the same states and same conditions as in Fig. 2, except that the lattice is suddenly shifted in position by $\lambda/4$ between Rydberg-atom preparation and modulated-lattice drive.

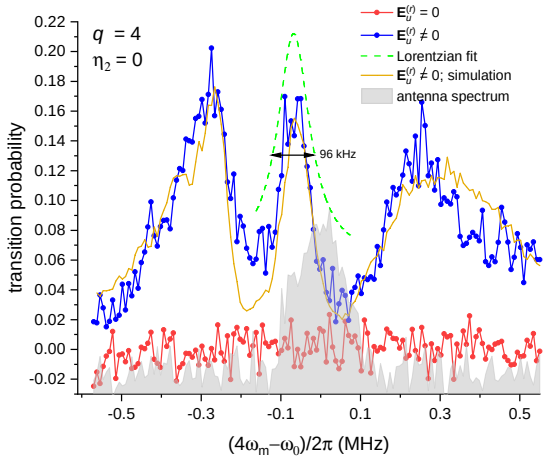


FIG. 4. Population in $|1\rangle$ as ω_m is scanned over $\omega_0/4$ in 2 kHz steps. In this spectrum, $|0\rangle = |48S_{1/2}\rangle$, $|1\rangle = |49S_{1/2}\rangle$, and $\omega_0/2\pi = 70.475710$ GHz. The blue signal is an average of 10 individual ω_m-scans with 400 measurements each and $\mathbf{E}_u^{(r)}$ unblocked. The green, dashed line is a Lorentzian fit of the Doppler-free, $\Delta\nu = 0$ line, revealing a linewidth of 96 kHz. The gold line represents a numerical simulation result scaled down by 50%, accounting for an inefficiency in state-selective detection. The pink signal shows the population in $|1\rangle$ when $\mathbf{E}_u^{(r)}$ is blocked for an average of 6 individual scans with 400 measurements each. The shaded spectrum shows a two-photon microwave drive using a horn antenna for $\tau = 6$ μs without any 1064-nm light.

potential while most of them are being captured in the translating lattice wells. We also note that the Doppler-free peak in Fig. 2 is blue-shifted; this is a result of a differential light shift between states $|0\rangle$ and $|1\rangle$ for atoms near standing-wave nodes [22, 23]

In both Figs. 2 and 3 the central Doppler-free components are broader than in the simulations, where the FWHM of the Doppler-free components is near the Fourier limit of ≈ 150 kHz. This excess broadening of the experimental Doppler-free components likely arises from the $46P_{1/2}$ hyperfine structure [24], stray magnetic fields, and possible Rydberg dipole-dipole interactions.

Next, we demonstrate Doppler-free ponderomotive lattice phase-modulation spectroscopy for Rydberg states $|0\rangle$ and $|1\rangle$ of same parity, which are not subject to line broadening from electric-dipole interactions. We choose $|0\rangle = |48S_{1/2}\rangle$ and $|1\rangle = |49S_{1/2}\rangle$. The sample is initialized in $|0\rangle$, for which our lattice potential has a half-depth $U_0 = h \times 2.5$ MHz. The phases η_0 and η_2 are set to zero, the sub-harmonic order is $q = 4$, and $\omega_m/2\pi$ is scanned from 17.618785 GHz to 17.619065 GHz in steps of 2 kHz. The modulation parameter η_1 is set such that the $q = 4$ peak coupling in Eq. (2),

$$\Omega_{4,0} = -\frac{\alpha_e(\omega_L)}{\hbar}\mathcal{E}_m^{(i)}\mathcal{E}_u^{(r)}(\hat{\epsilon}^{(i)}\cdot\hat{\epsilon}^{(r)}) \times \langle 1|\cos(2k_L z_e)|0\rangle J_4(\eta_1) \quad , \quad (5)$$

becomes large ($\Omega_{4,0} \sim 2\pi \times 90$ kHz for our case). The interaction time between atoms and the phase-modulated lattice is $\tau = 12$ μs.

Fig. 4 shows our results for the even-parity $|0\rangle \rightarrow |1\rangle$ spectrum. There are no transitions when blocking $\mathbf{E}_u^{(r)}$, which proves that the observed spectrum cannot be a high-order transition driven by stray microwave radiation, nor can it be an optical stimulated Raman transition driven by the remaining uni-directional, phase-modulated laser beam. A Lorentzian fit to the Doppler-free central peak has a FWHM linewidth of 96 kHz, which is in line with our Rabi-frequency estimate and the linewidth in the simulated spectrum. The small red-shift of the lattice-driven Doppler-free peak relative to the microwave reference peak, which is a two-photon transition, reflects a differential light shift between states $|0\rangle$ and $|1\rangle$ at the standing-wave maxima.

We finally discuss why Figs. 2-4 demonstrate a novel type of Doppler-free spectroscopy. Semi-classically, an atom moves on a trajectory $Z_0(t)$ as it is being probed. In spectroscopy based on the $\mathbf{A}\cdot\mathbf{p}$ interaction, the phase function usually is $\xi(Z_0) = \Delta k Z_0$, and the first-order Doppler effect is $\dot{\xi} = \Delta k v$. If atoms underwent a stimulated Raman transition (notably non-existent, in our work) in counter-propagating lattice beams with wavenumbers $\pm k_L$, there would be three branches of $\xi(Z_0)$, namely $\xi = 0$, corresponding to a Doppler-free spectral component, and $\xi = \pm 2k_L Z_0$, corresponding to spectral components with Doppler shifts $\pm 2k_L v$ [blue dashed lines in Fig. 1 (c)]. Whereas, lattice-trapped atoms probed by ponderomotive lattice-modulation spec-

troscopy remain on a single step of the staircase function in Fig. 1 (c) and sample the same phase at all times (trajectories 1), resulting in Doppler-free excitation, as in the Doppler-free component of a hypothetical Raman transition [horizontal blue dashed line in Fig. 1 (c)]. Untrapped atoms (trajectories 2) run over may steps, resulting in approximately the same Doppler effect as in the Doppler-shifted Raman transitions [diagonal blue dashed lines in Fig. 1 (c)]. It is thus concluded that lattice trapping and the peculiar staircase shape of $\xi(Z_0)$, which is unique to ponderomotive lattice modulation couplings, enable a novel type of Doppler-free spectroscopy.

In summary, we have observed both even- and odd-parity ponderomotive Rydberg transitions near the Fourier-limit using a phase-modulated optical lattice. Doppler- and recoil-free $|nS_{1/2}\rangle \rightarrow |n'P_{1/2}\rangle$ optically-driven Rydberg transitions, demonstrated here, are useful for spin manipulations in quantum simulators [3, 5], especially in protocols that require site-selective excitations. Doppler- and recoil-free $|nS_{1/2}\rangle \rightarrow |n'S_{1/2}\rangle$ transitions, also demonstrated here, are useful in high-precision spectroscopy where strong electric-dipole interactions between Rydberg atoms are to be avoided [25]. Optical couplings of Rydberg states free of the usual selection rules, afforded by ponderomotive lattice modulation spectroscopy, open access to higher-dimensional Hilbert spaces, including circular Rydberg states, allowing novel methods for quantum-state engineering and control [26–28]. Lattices in the synthetic dimension [20, 29] of the Rydberg internal-state space can also be generated using the ponderomotive light-matter interaction presented here. Lastly, in alkaline-earth Rydberg atoms, the ponderomotive interaction, at suitable frequencies, would enable selective addressing of the Rydberg electron, with the core electrons remaining spectators.

This work was supported by NSF Grant No. PHY-2110049. R.C. acknowledges support from the Rackham Predoctoral Fellowship.

* rcardman@umich.edu

[1] H. Bernien, S. Schwartz, A. Keesling, H. Levine, A. Omran, H. Pichler, S. Choi, A. S. Zibrov, M. Endres, M. Greiner, *et al.*, Nature **551**, 579 (2017).

[2] T. L. Nguyen, J. M. Raimond, C. Sayrin, R. Cortiñas, T. Cantat-Moltrecht, F. Assemat, I. Dotsenko, S. Gleyzes, S. Haroche, G. Roux, T. Jolicoeur, and M. Brune, Phys. Rev. X **8**, 011032 (2018).

[3] A. Browaeys and T. Lahaye, Nature Physics **16**, 132 (2020).

[4] P. Scholl, M. Schuler, H. J. Williams, A. A. Eberharter, D. Barredo, K.-N. Schymik, V. Lienhard, L.-P. Henry, T. C. Lang, T. Lahaye, *et al.*, Nature **595**, 233 (2021).

[5] M. Khazali, Quantum **6**, 664 (2022).

[6] M. Saffman, T. G. Walker, and K. Mølmer, Rev. Mod. Phys. **82**, 2313 (2010).

[7] S. R. Cohen and J. D. Thompson, PRX Quantum **2**, 030322 (2021).

[8] C. L. Holloway, J. A. Gordon, S. Jefferts, A. Schwarzkopf, D. A. Anderson, S. A. Miller, N. Thaicharoen, and G. Raithel, IEEE Transactions on Antennas and Propagation **62**, 6169 (2014).

[9] D. H. Meyer, Z. A. Castillo, K. C. Cox, and P. D. Kunz, Journal of Physics B: Atomic, Molecular and Optical Physics **53**, 034001 (2020).

[10] R. M. Jopson, R. R. Freeman, W. E. Cooke, and J. Bokor, Phys. Rev. Lett. **51**, 1640 (1983).

[11] R. R. Jones and T. F. Gallagher, Phys. Rev. A **38**, 2846 (1988).

[12] R. R. Jones, C. J. Dai, and T. F. Gallagher, Phys. Rev. A **41**, 316 (1990).

[13] H. Lehec, X. Hua, P. Pillet, and P. Cheinet, Physical Review A **103**, 022806 (2021).

[14] A. Muni, L. Lachaud, A. Couto, M. Poirier, R. C. Teixeira, J.-M. Raimond, M. Brune, and S. Gleyzes, Nature Physics **18**, 502 (2022).

[15] K.-L. Pham, T. F. Gallagher, P. Pillet, S. Lepoutre, and P. Cheinet, PRX Quantum **3**, 020327 (2022).

[16] A. P. Burgers, S. Ma, S. Saskin, J. Wilson, M. A. Alarcón, C. H. Greene, and J. D. Thompson, PRX Quantum **3**, 020326 (2022).

[17] K. R. Moore, S. E. Anderson, and G. Raithel, Nature communications **6**, 1 (2015).

[18] V. S. Malinovsky, K. R. Moore, and G. Raithel, Phys. Rev. A **101**, 033414 (2020).

[19] B. Knuffman and G. Raithel, Phys. Rev. A **75**, 053401 (2007).

[20] S. Kanungo, J. Whalen, Y. Lu, M. Yuan, S. Dasgupta, F. Dunning, K. Hazzard, and T. Killian, Nature communications **13**, 1 (2022).

[21] T. F. Gallagher, *Rydberg Atoms* (Cambridge University Press, Cambridge, 1994).

[22] S. E. Anderson, K. C. Younge, and G. Raithel, Phys. Rev. Lett. **107**, 263001 (2011).

[23] K. C. Younge, B. Knuffman, S. E. Anderson, and G. Raithel, Phys. Rev. Lett. **104**, 173001 (2010).

[24] R. Cardman and G. Raithel, arXiv preprint arXiv:2207.08582 (2022).

[25] A. Ramos, K. Moore, and G. Raithel, Phys. Rev. A **96**, 032513 (2017).

[26] R. Cardman and G. Raithel, Phys. Rev. A **101**, 013434 (2020).

[27] A. Larrouy, S. Patsch, R. Richaud, J.-M. Raimond, M. Brune, C. P. Koch, and S. Gleyzes, Phys. Rev. X **10**, 021058 (2020).

[28] A. Signoles, E. K. Dietsche, A. Facon, D. Grosso, S. Haroche, J. M. Raimond, M. Brune, and S. Gleyzes, Phys. Rev. Lett. **118**, 253603 (2017).

[29] C. Feng, H. Manetsch, V. G. Rousseau, K. R. A. Hazzard, and R. Scalettar, Phys. Rev. A **105**, 063320 (2022).

arXiv:2210.01874v1 [physics.atom-ph] 4 Oct 2022

Supplemental Material for "Driving alkali Rydberg transitions with a phase-modulated optical lattice"

R. Cardman* and G. Raithel
Department of Physics, University of Michigan, Ann Arbor, MI 48109, USA
(Dated: October 6, 2022)

METHODS

Spectroscopy Laser

The laser used for probing the ponderomotive Rydberg-Rydberg transitions is a narrow-linewidth (< 100 kHz) Nd:YAG fiber laser (IPG Model YLR-10-1064-LP-SF) that produces up to 10 W of optical power. While the frequency output of the laser is very stable, it is not tunable, meaning external electro-optic devices and servo-controlled opto-mechanics are necessary for controlling phases η_0 and η_2. Optics and electronics necessary for phase-stabilization and shifting are sketched in Fig. S1.

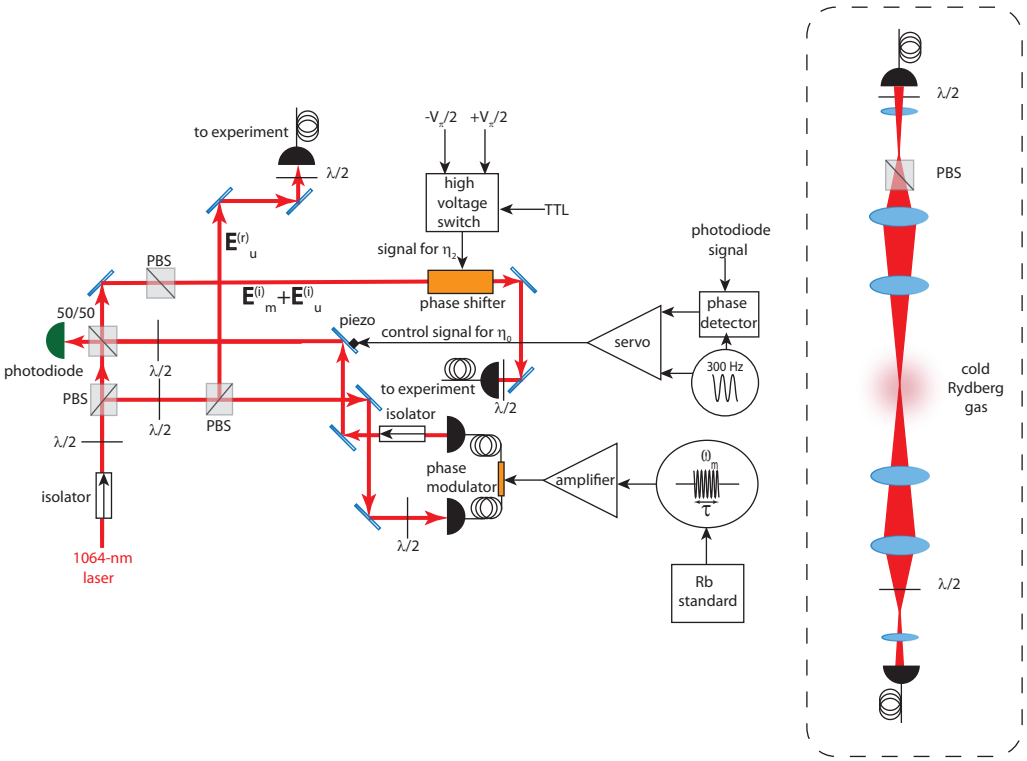


Figure 1. Optical schematic of 1064-nm spectroscopy laser used for driving the Rydberg-Rydberg transitions through phase modulation. Here, "λ/2" indicates a half-wave plate, "50/50" indicates a 50:50 beamsplitter, and "PBS" indicates a polarizing beamsplitter. The inset presents the shaping and alignment of the beam, as it is focused at the center of the Rydberg atom sample.

The phase-modulated beam $\mathbf{E}_m^{(i)}$ is realized by sending light through a low-V_π, broadband fiber phase modulator (iXblue Model NIR-MPZ-LN-20) of a lithium niobate crystal [1]. A signal generator referenced to a Rb standard (SRS Model FS725) provides pulse-modulated microwaves of frequency ω_m that are amplified to reach an appropriate value of η_1 and fed into the phase modulator. The phase-shaken light is mode matched with an unmodulated beam $\mathbf{E}_u^{(i)}$ on a photodiode (PD) that is used for the generation of an error signal to control a piezo-actuated mirror such that η_0 remains stabilized. The phase η_0 is stabilized and fixed to zero by peak-locking the piezo to a Mach-Zehnder fringe maximum detected by the the PD. Both beams, now coherently added, are sent through another free-space

phase-modulator (ConOptics Model M350-105) with a much higher V_π and lower bandwidth. This device is used as a dc phase shifter that controls η_2, the relative phase between counter-propagating beams. We couple these incident i beams through an optical fiber to our to experiment and attain 880 mW for field $\mathbf{E}_u^{(i)}$ and 12 mW for field $\mathbf{E}_m^{(i)}$.

Control of η_2 is necessary in the lattice-intensity inversion experiment of the $|46S_{1/2}\rangle \rightarrow |46P_{1/2}\rangle$ transition. The inversion is provided by applying a potential differences to the phase-shifter right before the phase modulation is pulsed on for interaction time τ. A potential difference near V_π translates to an overall phase shift of $\eta_2 = \pi$ that inverts the optical lattice forces [2]. The high-voltage switching is performed with a DEI Model PVX-4150 Pulse Generator gated with an external TTL pulse.

The second unmodulated beam $\mathbf{E}_u^{(r)}$ that counter-propagates $\mathbf{E}_m^{(i)} + \mathbf{E}_u^{(i)}$ is sent directly through a fiber to the experiment yielding 940 mW of coupled light. All beams are enlarged to a diameter of ~ 1 cm and focused down to a waist of ~ 15 μm at the interaction region of our cold Rydberg atom sample. The fiber coupling provides a spatial mode filter for all beams as well as an alignment tool. Once an optimized free-running, single-beam dipole trap is established with the incident beams i by placing the focusing lens in the right position, the return beam r can be sufficiently overlapped to form a standing wave by measuring the coupling efficiency of $\mathbf{E}_u^{(r)}$ through the incident fiber.

Rydberg State Preparation

A Rb oven generates a thermal gas of the alkali that is directed into a vapor-cell 2D$^+$-MOT chamber [3]. A cold ^{85}Rb beam is generated in this chamber by near-resonant cycling-transition and repumping light. This atomic beam is then transferred to the science chamber where polarization-gradient cooling in the σ^+-σ^- configuration is performed [4]. The 1064-nm light is CW and never switched off throughout the experiment, only the modulation signal $\eta_1 \cos(\omega_m t)$ is pulsed. Thus, cooling occurs for atoms trapped in the intensity-peaks of the optical lattice.

After the cooling light is switched off, simultaneous 780- and 480-nm laser pulses excite the $5S_{1/2}$ atoms trapped in the intensity maxima of the 1064-nm lattice into the Rydberg state $|0\rangle$. These atoms can be selectively excited by detuning the 480-nm laser by the maximum light shifts induced on $|0\rangle$ and $|5S_{1/2}\rangle$. We set the frequency of the 480-nm laser at the peak of the rightmost-feature in Fig. S2. The 780-nm laser is blue-detuned from the $|5P_{3/2}; F' = 4\rangle$ state by $\Delta = +140$ MHz to reduce the photon-scattering rate. Both lasers are on for a duration of 4 μs. in order to reduce the number of detected atoms that are not trapped by 1064-nm laser light, we co-align the 780-nm beam with the incident 1064-nm beams and angle the 480-nm laser 60° from the 780/1064-nm beams.

After the Rydberg-excitation lasers are switched off, the modulation pulse is switched on to induce $|0\rangle \rightarrow |1\rangle$ transitions. Optionally, before the rise time of the modulation pulse, a voltage of V_π applied to the phase shifter that controls η_2 can be switched on, inverting the lattice's intensity gradient.

Determining ω_0

The frequency axes of all spectra presented in this work are referenced to the lattice-free transition frequencies $\omega_0/2\pi$ between $|0\rangle$ and $|1\rangle$. We can measure these frequencies with one- and two-photon mm-wave spectroscopy of the Rydberg atoms and check for broadening from dc-Stark and Zeeman effects. The mm-waves are fed directly from the signal generator to a 20 dBi horn antenna located 30 cm from the optical molasses outside of the science chamber. State-selective field ionization (SSFI) is used in all experiments to discern the number of atoms in $|0\rangle$ versus $|1\rangle$, by only counting the number of ions arriving at the microchannel plate detector (MCP) within a specified time window by a single-particle counter (SRS Model SR400) [5].

In Fig. S3(a), we show single-photon mm-wave spectroscopy of the $|46S_{1/2}\rangle \rightarrow |46P_{1/2}\rangle$ transition and a Lorentzian fit with line center $\omega_0/2\pi = 39.121294(3)$ GHz. In Fig. S3(b), two-photon mm-wave spectroscopy is performed on the $|48S_{1/2}\rangle \rightarrow |49S_{1/2}\rangle$ transition, revealing a transition frequency of $\omega_0/2\pi = 70.475710(3)$ GHz from a Lorentzian fit.

THEORY & SIMULATION

In this section, we show the derivation of the optical lattice potential $U_0 \cos(2k_L Z_0)$ and atom-field coupling U_{AF}, and we present a description of the numerical simulator for our experimental spectra.

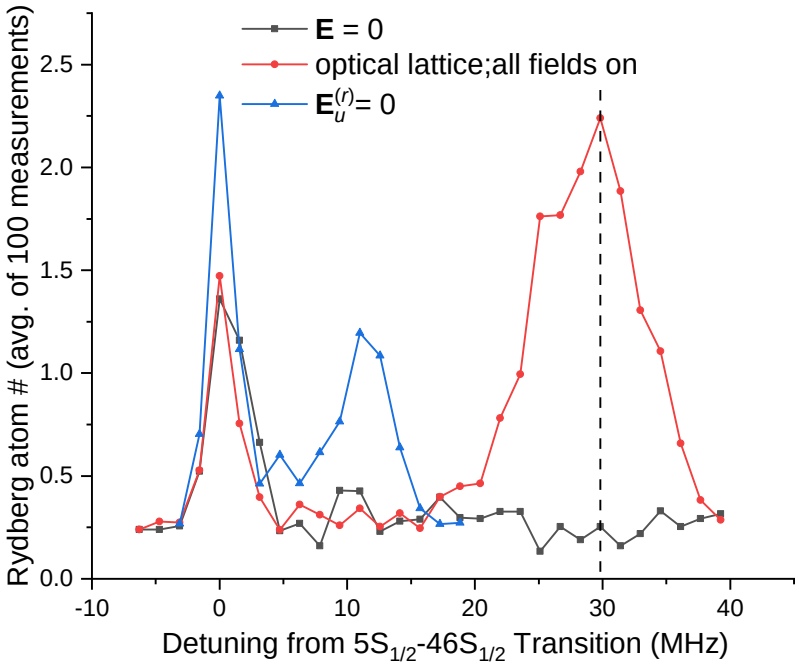


Figure 2. Light shifts on transition frequency for $5S_{1/2} \rightarrow 46S_{1/2}$ optical excitation. The cases where there is no 1064-nm light ($\mathbf{E} = 0$), no return field ($\mathbf{E}_u^{(r)} = 0$), and a 1064-nm optical lattice formed by all three fields, $\mathbf{E}_m^{(i)}, \mathbf{E}_u^{(i)}$, and $\mathbf{E}_u^{(r)}$, are shown. The dashed line indicates where the detuning of the 480-nm laser is typically set during an experimental run.

Derivation of Optical Lattice Potential and Rabi Frequencies

In the Hamiltonian for the Rydberg-electron with coordinate $\mathbf{r}_e$, the ponderomotive interaction arising from the quasi-free electron's quiver motion in the laser field of angular frequency ω_L yields and ac-Stark-like potential

$$U_p(\mathbf{R}_0 + \mathbf{r}_e, t) = -\frac{1}{2}\alpha_e(\omega_L)\langle \mathbf{E}^2(\mathbf{R}_0 + \mathbf{r}_e, t)\rangle_{t_q}, \tag{1}$$

where the angled brackets indicate a time average over several quiver periods t_q of the electron ($t_q = 2\pi/\omega_L$). Here, α_e is the free-electron polarizability (-545 atomic units for 1064-nm). After finding the mean-square of the net laser field, which is $\mathbf{E} = \mathbf{E}_m^{(i)} + \mathbf{E}_u^{(i)} + \mathbf{E}_u^{(r)}$ in the context of this experiment, we find that

$$\begin{aligned}\langle \mathbf{E}^2(\mathbf{R}_0 + \mathbf{r}_e, t)\rangle_{t_q} &= \frac{1}{2}[\mathcal{E}_m^{(i)}]^2 + \frac{1}{2}[\mathcal{E}_u^{(i)}]^2 + \frac{1}{2}[\mathcal{E}_u^{(r)}]^2 + \mathcal{E}_m^{(i)}\mathcal{E}_u^{(i)}\cos\left[\eta_0 + \eta_1\cos\left(\omega_m\Delta s/c - \omega_m t\right)\right] \\ &+\mathcal{E}_m^{(i)}\mathcal{E}_u^{(r)}(\hat{\epsilon}^{(i)}\cdot\hat{\epsilon}^{(r)})\cos\left[2k_L(Z_0 + z_e) + \eta_0 + \eta_1\cos\left(\omega_m\Delta s/c - \omega_m t\right) + \eta_2(t)\right] + \mathcal{E}_u^{(i)}\mathcal{E}_u^{(r)}(\hat{\epsilon}^{(i)}\cdot\hat{\epsilon}^{(r)})\cos\left[2k_L(Z_0 + z_e) + \eta_2(t)\right],\end{aligned} \tag{2}$$

where $\hat{\epsilon}^{(i)}, \hat{\epsilon}^{(r)}$ are linear polarization vectors, ω_m is the phase modulation frequency, and Δs is the path length difference of modulation from its generation in the synthesizer to the location of the atoms.

The optical lattice potential is determined from first-order nondegenerate perturbation theory of the Rydberg electron by the time-independent part of the U_p term in the Hamiltonian. Thus,

$$\left\langle \frac{-1}{2}\alpha_e(\omega_L)\mathcal{E}_u^{(i)}\mathcal{E}_u^{(r)}(\hat{\epsilon}^{(i)}\cdot\hat{\epsilon}^{(r)})\cos\left[2k_L(Z_0 + z_e) + \eta_2\right]\right\rangle = -\frac{1}{2}\alpha_e(\omega_L)\mathcal{E}_u^{(i)}\mathcal{E}_u^{(r)}(\hat{\epsilon}^{(i)}\cdot\hat{\epsilon}^{(r)})\langle\cos\left(2k_L z_e\right)\rangle\cos\left(2k_L Z_0 + \eta_2(t)\right), \tag{3}$$

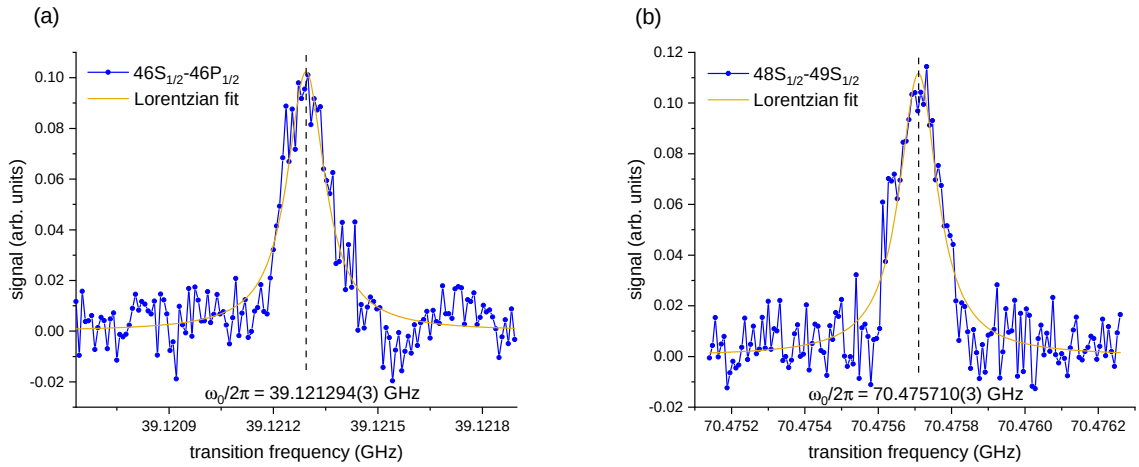


Figure 3. In (a), we measure ω_0 for the $46S_{1/2} \rightarrow 46P_{1/2}$ transition with no 1064-nm light applied using single-photon, mm-wave spectroscopy with a horn antenna. In (b), we measure ω_0 for the $48S_{1/2} \rightarrow 49P_{1/2}$ transition without the lattice light using two-photon, mm-wave spectroscopy with the same horn antenna.

where $\langle \cos(2k_L z_e) \rangle$ is a state-dependent matrix element that is 0.553, 0.537, 0.485, and 0.450 for $|46S_{1/2}\rangle$,$|46P_{1/2}\rangle$,$|48S_{1/2}\rangle$, and $|49S_{1/2}\rangle$ respectively. The state-dependent, lattice-well half depth U_0 is

$$U_0 = -\frac{1}{2}\alpha_e(\omega_L)\mathcal{E}_u^{(i)}\mathcal{E}_u^{(r)}(\hat{\epsilon}^{(i)} \cdot \hat{\epsilon}^{(r)})\langle \cos(2k_L z_e) \rangle. \tag{4}$$

Even though the ponderomotive potential term proportional to $\mathcal{E}_m^{(i)}\mathcal{E}_u^{(i)} \cos[\eta_0 + \eta_1 \cos(\omega_m \Delta s/c - \omega_m t)]$ conserves energy in the electronic transition from $|0\rangle$ to $|1\rangle$, it does not conserve angular momentum, as there is no significant dependence on the vector operator $\mathbf{r}_e$. However, the term arising from two counterpropagating fields of different frequencies conserves both angular momentum and energy. Proper expansion of this term, where $\eta_0 = 0$ in this experimental context yields a spatially dependent atom-field interaction that can couple motional Rydberg states ν having the same parity and internal states $|0\rangle$ and $|1\rangle$ with either the same or different parity depending on the choice of the harmonic q:

$$U_{AF}(Z_0,t) = -\frac{1}{2}\alpha_e \mathcal{E}_m^{(i)}\mathcal{E}_u^{(r)}(\hat{\epsilon}^{(i)} \cdot \hat{\epsilon}^{(r)}) \cos(2k_L Z_0 + \eta_2(t)) \Bigg\{ \langle 1| \cos(2k_L z_e) |0\rangle$$
$$\times \left[J_0(\eta_1) + 2 \sum_{\text{even } q>0} J_q(\eta_1) \cos(q\omega_m \Delta s/c - q\omega_m t) \right] + \langle 1| \sin(2k_L z_e) |0\rangle \left[2 \sum_{\text{odd } q} J_q(\eta_1) \sin(q\omega_m \Delta s/c - q\omega_m t) \right] \Bigg\}$$
$$\times (|1\rangle\langle 0| + |0\rangle\langle 1|). \tag{5}$$

The term $q\omega_m \Delta s/c$ provides a constant phase; under the rotating-wave approximation (RWA),

$$U_{AF}(Z_0,t) = \frac{\hbar}{2}\Omega_{q,0} |\cos(2k_L Z_0)| e^{i(\xi - q\omega_m t)} |1\rangle\langle 0| + \text{h.c.}, \tag{6}$$

where

$$\Omega_{q,0} = -\frac{\alpha_e(\omega_L)}{\hbar}\mathcal{E}_m^{(i)}\mathcal{E}_u^{(r)}(\hat{\epsilon}^{(i)} \cdot \hat{\epsilon}^{(r)}) \langle 1| \sin(2k_L z_e) |0\rangle J_q(\eta_1), \tag{7}$$

for odd-parity transitions and

$$\Omega_{q,0} = -\frac{\alpha_e(\omega_L)}{\hbar}\mathcal{E}_m^{(i)}\mathcal{E}_u^{(r)}(\hat{\epsilon}^{(i)} \cdot \hat{\epsilon}^{(r)}) \langle 1| \cos(2k_L z_e) |0\rangle J_q(\eta_1), \tag{8}$$

for even-parity transitions. The overall phase ξ ends up having a staircase-function dependence on Z_0 that steps π every $\lambda/4$. When $\eta_2(t)$ shifts by amount π, this staircase function shifts upwards by the same amount.

Numerical Simulation

In our simulation of observed spectra, we treat the Rydberg atom's center-of-mass (CM) coordinate classically, meaning that a quantum interpretation of quantized motional states ν having a Bloch wave function is ignored in the program. The calculated spectrum is an average of 1000 classical atomic trajectories for each ω_m. The initial positions $Z_0(t=0)$ and velocities $\dot{Z}_0(t=0)$ follow a Maxwell-Boltzmann distribution for temperature T_0 in the lattice for the $5S_{1/2}$ ground state. The lattice can undergo a shift η_2 that effectively translates the initial positions $Z_0(t=0)$ of the atoms relative to the lattice.

For a single trajectory at a specified modulation frequency ω_m, the position $Z_0(t)$ determines the atom-field coupling and the modulation-frequency detuning versus time. Since the transitions in this work are non-magic, the acceleration of the classical CM coordinate, $\ddot{Z}_0(t)$, due to the adiabatic potential of the lattice is averaged over both states, using the internal-state populations as weighting factors. A Runge-Kutta algorithm propagates the CM coordinates $Z_0, \dot{Z}_0$ according to the classical equations of the CM motion, using a time step Δt. The Rabi frequencies and detunings depend on t through Z_0. The quantum subroutine uses the time-dependent Rabi frequencies and detunings as an input and propagates the state coefficients for $|0\rangle$ and $|1\rangle$. The simulation of one trajectory ends when the desired atom-field interaction duration τ is reached. The final probabilities for $|0\rangle$ and $|1\rangle$ are recorded. Typically, the resultant transition probabilities are averaged over 1000 simulated trajectories, for each value of ω_m sampled.

In Fig. S4, we explore the behavior of simulated spectra as experimentally accessible parameters $U_0, \Omega_{4,0}$, and T_0 are varied for $|0\rangle = \left|48S_{1/2}\right\rangle$ and $|1\rangle = \left|49S_{1/2}\right\rangle$, as an example. We can estimate U_0 in our experiment by comparing the experimental and calculated splittings among the three peaks at a fixed initial temperature T_0 and Rabi frequency peak amplitude $\Omega_{q=4,0}$. Once U_0 is determined, the Rabi frequency can be varied with U_0 and T_0 fixed to match the relative heights among the three peaks that we experimentally observe. The third map demonstrates the spectrum's behavior as the initial temperature is varied. For all three simulated maps, the interaction time is $\tau = 12$ μs.

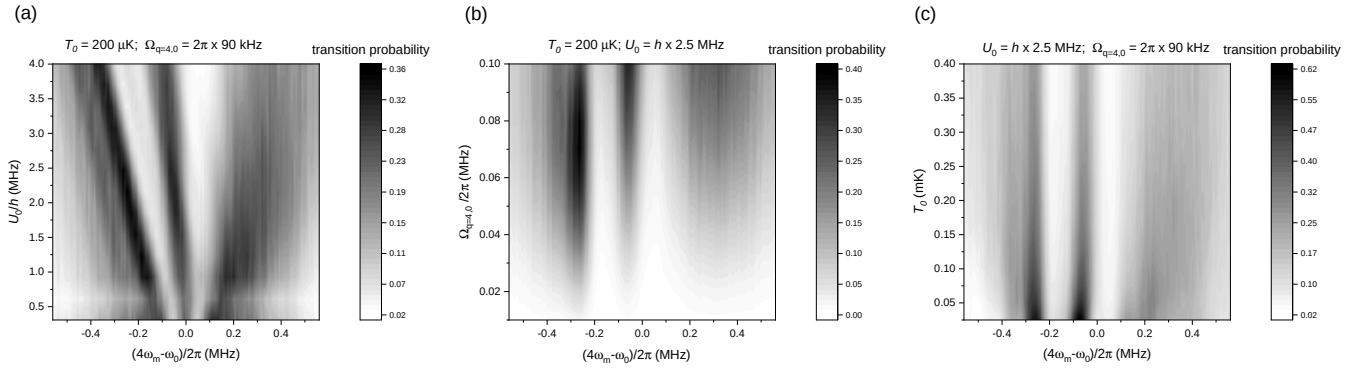


Figure 4. In (a), we fix $T_0 = 200$ μK, $\Omega_{4,0} = 2\pi \times 90$ kHz and vary U_0 in a simulation of the $\left|48S_{1/2}\right\rangle \rightarrow \left|49S_{1/2}\right\rangle$ transition. For (b), we fix $T_0 = 200$ μK, $U_0 = h \times 2.5$ MHz and vary $\Omega_{4,0}$; for (c), we fix $U_0 = h \times 2.5$ MHz and $\Omega_{4,0}$ and vary T_0.

* rcardman@umich.edu

[1] A. Yariv and P. Yeh, *Optical waves in crystals*, Vol. 5 (Wiley New York, 1984).
[2] S. E. Anderson, K. C. Younge, and G. Raithel, Phys. Rev. Lett. **107**, 263001 (2011).
[3] K. Dieckmann, R. J. C. Spreeuw, M. Weidemüller, and J. T. M. Walraven, Phys. Rev. A **58**, 3891 (1998).

[4] J. Dalibard and C. Cohen-Tannoudji, JOSA B **6**, 2023 (1989).
[5] T. F. Gallagher, *Rydberg Atoms* (Cambridge University Press, Cambridge, 1994).